Available online at www.sciencedirect.com

ScienceDirect

Ceramics International 41 (2015) 8320–8330

CERAMICS INTERNATIONAL

www.elsevier.com/locate/ceramint

Effect of layer printing delay on mechanical properties and dimensional accuracy of 3D printed porous prototypes in bone tissue engineering

Arghavan Farzadi[a,*], Vicknes Waran[b], Mehran Solati-Hashjin[a], Zainal Ariff Abdul Rahman[c], Mitra Asadi[a], Noor Azuan Abu Osman[a]

[a]Department of Biomedical Engineering, Faculty of Engineering, University of Malaya, 50603 Kuala Lumpur, Malaysia
[b]Division of Neurosurgery, Faculty of Medicine, University of Malaya, Kuala Lumpur, Malaysia
[c]Oral Cancer Research Team; Cancer Research Initiatives Foundation (CARIF), Subang Jaya, Selangor, Malaysia

Received 15 November 2014; received in revised form 13 February 2015; accepted 2 March 2015
Available online 9 March 2015

Abstract

Recent advancements in computational design and additive manufacturing have enabled the fabrication of 3D prototypes with controlled architecture resembling the natural bone. Powder-based three-dimensional printing (3DP) is a versatile method for production of synthetic scaffolds using sequential layering process. The quality of 3D printed products by this method is controlled by the optimal build parameters. In this study, Calcium Sulfate based powders were used for porous scaffolds fabrication. The *X*-direction printed scaffolds with a pore size of 0.8 mm and a layer thickness of 0.1125 mm were subjected to the depowdering step. The effects of four layer printing delays of 50, 100, 300 and 500 ms on the physical and mechanical properties of printed scaffolds were investigated. The compressive strength, toughness and tangent modulus of samples printed with a delay of 300 ms were observed to be higher than other samples. Furthermore, the results of SEM and μCT analyses showed that samples printed with a delay of 300 ms have higher dimensional accuracy and are significantly closer to CAD software based designs with predefined 0.8 mm macro-pore and 0.6 mm strut size.

Keywords: Additive manufacturing; 3D printing; Dimensional accuracy; Compressive strength; Delay in printing

1. Introduction

The formation of a porous structure is the primary objective in bone scaffold fabrication. A number of techniques have been developed to achieve this purpose including the phase separation, the gas foaming, the solvent casting particulate leaching, and the freeze drying. Most of these techniques are still commonly used due to their relative simplicity but exploit organic solvents during the process to dissolve synthetic polymers. The presence of organic solvent residues can create significant problems in conventional fabrication methods [1–6]. Furthermore, a core limitation of such technologies is the lack of precise control over scaffold specifications such as pore size, shape, distribution, and interconnectivity. Such specifications also include the overall scaffold shape and the porosity of the material [1,6,7].

As an alternative to conventional scaffold fabrication methods, a new class of techniques called rapid prototyping (RP) or solid free form fabrication (SFF) techniques has recently emerged in the tissue engineering industry. According to the ASTM F2792-12a (Standard Terminology for Additive Manufacturing), rapid prototyping and solid free form fabrication methods have been replaced with Additive Manufacturing method (AM). The AM technology is a common name for a number of advanced manufacturing techniques that are based on an additive process in that complex structures are constructed in a layer-by-layer fashion according to a computer program [8–16]. All the AM techniques are based on the use of computer-aided design (CAD) information represented in a.STL type file format. The name is derived from the stereolithography, the oldest of the AM technologies. The STL file format has been accepted as the

*Corresponding author. Tel.: +60 1123288082.
E-mail address: arghavan@um.edu.my (A. Farzadi).

http://dx.doi.org/10.1016/j.ceramint.2015.03.004

golden standard in the industry. The CAD data is converted into a series of cross-sectional layers [17–19]. These computer generated two-dimensional layers are then created as a solid model by a variety of processes. Starting from the bottom and proceeding upwards, each layer is glued or otherwise bonded to the previous layer constructing a solid model of the object presented on the computer screen. In addition, the data obtained from computerized tomography (CT) or magnetic resonance imaging (MRI) scans can also be used to create customized CAD models. In this approach, first the desired implant area of the patient is scanned by CT or MRI and then the resulting data is imported into the CAD software. The software enables a surgeon to design an implant according to the individual's needs. After the information is transferred to a AM system, a biocompatible and biodegradable scaffold is fabricated [8,20–22].

Over the past two decades more than 20 additive manufacturing systems such as Selective Laser Sintering (SLS), Fused Deposition Modeling (FDM), Stereolithography (SL) and three-dimensional printing (3DP) have been developed and commercialized. The selection of material choices ranges from variety of polymers, ceramics, metals and composites [8,11,23,24]. The technique of 3D printing consists of applying a layer of powder onto a surface and using an inkjet printer head to precisely spray the surface with a binder to bind the powder particles. The process is repeated by spreading a new layer of powder on top of the previous layer that results in the creation of a 3D structure [8,21–23,25–27].

Dimensional accuracy of a component part represents the degree of agreement between the manufactured dimension and its designed specification. This is the most critical factor in ensuring dimensional repeatability of manufactured component parts in bone tissue engineering. The resolution and accuracy of porous 3DP prototypes are determined by many factors such as materials used, printing delay, build orientation, print head resolution, geometric features and their topology, post treatment procedures, binder drop volume, binder–powder interaction, particle size and layer thickness. Unfortunately, the research attempts to determine such effects are often hampered by the constraints set by the commercial printers. In order to find a breakthrough in 3DP for scaffold engineering, both the accuracy (the mismatch between the model and the 3DP specimen) and the resolution (smallest feature size) need to be substantially improved [28,29].

The objective of this research project is to investigate the effect of layer printing delay on mechanical properties and dimensional accuracy of porous parts produced by the 3D printing process. According to current dimensioning and tolerating standards, the dimensional accuracy of a component part is evaluated through its size and shape by changing the printing parameters. This includes, the delay time in layer printing for each step and finding out the effect of such changes on the formation of the microarchitecture including pore size and shrinkage of the final parts [28,30,31].

After printing, the printed samples are usually post hardened or dip coated for maximum strength. In this research, the binder infiltration and post hardening were intentionally ignored to investigate the unconditional effect of printing delay on dimensional accuracy and common mechanical properties such as the compressive strength, tangent modulus and compressive toughness of the printed prototypes.

2. Methodology

2.1. Materials and methods

In this study, plaster based powder (zp150) with an appropriate water based binder solution of 2-Pyrrolidone (zb63) were used as the raw materials. The powder ZP150 is recommended for the accuracy and producing delicate models. It is a calcium sulfate based powder and was used in our experiments without any further sieving. The 3DP machine (Z450, Z Corporation, USA) is equipped with a number of useful features, such as automated setup and self-monitoring, automated powder loading, and automated powder recycling and removal. The printer has a specified resolution of 300×450 dpi^2 and a build size of $203 \times 254 \times 203$ mm^3. Furthermore, the thickness of selected build layer was 0.1125 mm. The test samples were prepared in a printer with ZPrint software version 7.9.2-4.

2.2. Specimen preparation

The ZP150 powders were loaded into a 3DP machine. The ZP450 prints a binder fluid through the conventional ink-jet print head into a powder, one layer onto another, from the lowest cross-section of the model to the highest. Tables 1 and 2 show the structural specifications of the printed samples designed by Solidworks CAD software and the 3DP fabrication condition, respectively. Printing was performed with binder/volume ratios of 0.24 (shell) and 0.12 (core) and with a saturation level of 100%. The values of binder/volume ratios for shell and core regions were assumed constant and the same test setup was used for all the samples. After printing, the printed models are dried in a building box for 1.5 h before removal from the powder bed. Then the samples were depowdered by compressed air to remove any unbound and trapped powders. Fig. 1 shows the Solidwork design and the 3D printed sample.

Table 1
Structural specification of samples designed by solidworks.

Shape	**Size of samples (mm)**	**Macro pore size (mm)**	**Strut size (mm)**
Cylinder	Diameter = 6 Height = 12	0.8	0.6
Volume of the full cylinder (mm^3)	**Volume of the porous cylinder (mm^3)**	**Porosity (Macro Pores) (%)**	**Specific Surface Area (mm^2)**
339.29	152.84	45.04	812.21

According to our previous work and the results presented in Table 3, layers were printed with different delay times in the *X* direction with a layer thickness of 0.1125 mm [29]. Four possible delay values of 50, 100, 300 and 500 ms were selected in for printing layers. The 100 ms delay is set as the default value for the printer.

2.3. Compositional, physical and mechanical characteristics of printed structures

Powder X-ray diffraction (XRD) characterization was carried out using a DKSH Technology (DY/032 Germany, Cu-Kα radiation, 40 kV, 30 mA and $0.02^{\circ}\ s^{-1}$ step scan). The software programs used to obtain the XRD patterns include OriginLab OriginPro v9.0 SR2 and PeakFit v.4.12. JCPDS files were used to identify the peaks of the main components in samples. The distribution curve (Cumulative distribution and Probability density function) of the particle size for starting calcium sulfate powders used for printing the samples was obtained from the particle size analyzer (Mastersizer MV version, Malvern Instrument Ltd.). Water was used as the medium since it does not have any side effects on the calcium sulfate particles.

Table 2
Fabrication condition of samples.

Saturation level (%)	Bleed compensation (mm)	Anisotropic scaling	Feature clearance (mm)
Shell: 100 Core: 100	*X*: 0.1778 *Y*: 0.1067 *Z*: 0.0254	*X*,*Y*, *Z*: 1, 1, 1	3.81

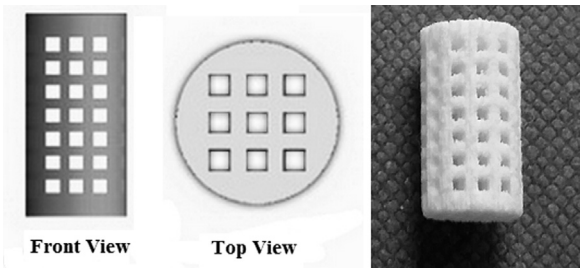

Fig. 1. Scaffold design (front and top views) using solidworks and 3D printed specimen.

Dimensions of printed samples were measured using a digital caliper (Mitutoyo model CD-6″CS, with 0–150 mm measurement range and 0.01 mm accuracy), and 24 measurements were taken twice at a 1 mm height step.

Uniaxial compression tests were conducted using a mechanical testing instrument (Instron 5848 Micro Tester, USA) with a 10 KN load cell and a crosshead-loading rate of 0.5 mm min^{-1}. Five cylinders of each type with 6 mm in diameter and 12 mm in height were used for this investigation [29,32–35]. The tangent modulus, compressive toughness and strength were calculated using the initial slope of linear region, the surface area under the curve and maximum compressive stress recorded in the stress–strain curve, respectively.

The microstructures of the finished parts and the average pore and strut size were calculated from pictures by scanning electron microscopy, SEM (Quanta FGG 250, Holland). Furthermore, the μCT analysis (SkyScan In-Vivo XRay 1076, Belgium), as a powerful investigative and non-destructive testing method, was used to characterize the porosity, pores interconnectivity and depowdering efficiency of printed scaffolds. The scanner used in experiments is a high resolution and compact desktop unit. The experiment setup is primarily designed for scans and also includes the associated control, reconstruction (NRecon, Skyscan) and analysis (CTAn/CTVol, Skyscan) software. The resolution for both groups of samples was set at 18 μm with a 0.5 mm aluminum filter and the rotation angle of 180°. Approximately 675 scan slices were taken and the scan files were reconstructed using a modified Feldkamp algorithm provided by Skyscan. The ability to differentiate between bone (Object) and soft tissue (VOI) works equally well when differentiating between the 3DP samples and open pore space in porous scaffolds [36].

2.4. Statistical analysis

Data collected from all experimental tests for dimensional accuracy investigation were evaluated using a one-way Analysis of Variance (ANOVA). ANOVA is performed to determine the significance of testing on three or more sample groups. The analysis consolidates all of the data into one number and gives one p value for the null hypothesis. The objective of variance analysis is to find the important independent variables and determine how they affect the response. In this research, a one-way ANOVA is used to determine the significance and a value of $p < 0.05$ was considered to be significantly different [37].

Table 3
Different delay in printing of samples.

Name of Samples	Delay in layer printing (ms)	Orientation	Layer thickness (mm)
S_{50}	50	*X*	0.1125
S_{100}	100		
S_{300}	300		
S_{500}	500		

3. Results and discussion

3.1. Chemical composition

The XRD spectrum of the 3D printed samples was analyzed. As shown in Fig. 2, the 3DP components consisted of single phase of Calcium Sulfate Semihydrate, with chemical formula of $CaSO_4.0.5 \cdot H_2O$, according to ICDD card No. 24-1067. There was no additional phase detected from the XRD analysis. This plaster has excellent printability in ink-jet 3DP manufacturing. Mixing $CaSO_4$ with water activates a self-hydration reaction that leads to recrystallization into a solid form of gypsum [15]. $CaSO_4$ based powders have been proved as an effective substitute for bone grafts and also enhancing new bone formation. However the use of such materials has been gradually substituted by HA due to weak strength and rapid resorption. Prior to the 3DP manufacturing of constructs from a bioceramics used for bone regeneration, it is critical to review the characteristics that influence the 3D printability of powders. In addition to the effect of materials type and fabrication cost reduction, the reproducibility and capability of porous structure with high dimensional accuracy and optimum mechanical properties have been investigated.

3.2. Particle size distribution

The differential distribution histogram of ZP150 powder particle sized used for 3D printing of samples is shown in Fig. 3. The curve obtained by the Malvern particle size analyser indicates a distribution with median diameter (d_{50}) of 27 μm and also, 69 μm, 48 μm, 8 μm and 0.64 μm representing d_{90}, d_{75}, d_{25} and d_{10} respectively. Powder with a relatively low particle size has the advantage of being easily removed. Thin layers are usually preferred in order to achieve a relatively higher level of resolution. However, it is also recommended that the layers should be thicker than the largest particle size of the powder [38]. Taking all that into account and from the results of our previous study, layer thickness of 0.1125 mm was chosen for this study since the powder particles used in our experiments had a d_{90} value of 69 μm.

3.3. Dimensional measurement

According to Fig. 4(a) and Table 4, the diameters of all printed samples were less than design values from CAD software (6 mm). The S_{300} and S_{500} samples had the close diameter to the CAD designed diameter. Also, the diameters of these samples (S_{300} and S_{500}) were the same. The S_{50} samples had the least diameter with the most deviation compared with the CAD designed diameter. In general, all S_{300} and S_{500} samples have the most considerable accuracy in dimension compared to CAD design.

According to Fig. 4(b), the height of all samples shrank with respect to CAD design (12 mm). Based on these results, S_{300} and S_{500} samples had the smallest difference in height compared to CAD designed heights while S_{50} and S_{100} samples had the highest difference in height. Also the height

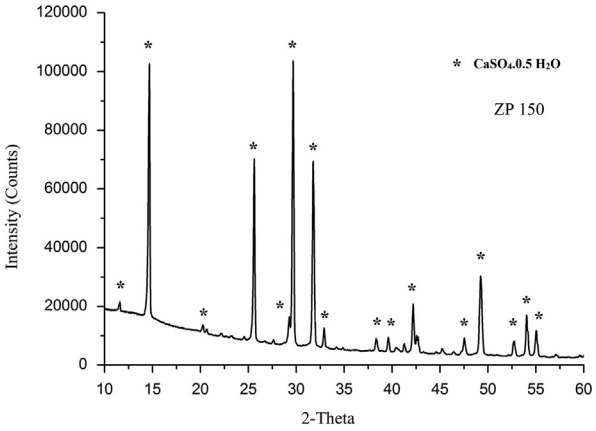

Fig. 2. XRD pattern of ZP150 powder, calcium sulfate semihydrate.

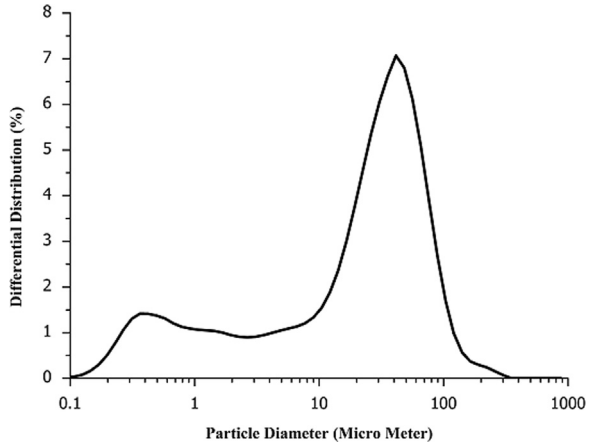

Fig. 3. Differential particle size distribution of ZP150, calcium sulfate semihydrate.

of S_{300} and S_{500} samples were very similar. 3D printed porous samples, allowing the part to absorb binder potentially causing the part to shrink and change dimensions. Furthermore, 3D printers produced parts that continue to change properties and dimensions over time or in varying environmental conditions such as ambient temperature and humidity. Furthermore, binder solidification is generally involved during layer formation, and this phase change from liquid to solid inevitably leads to shape shrinkage, and shape inaccuracy [39,40].

A correction to theses dimensional differences can be prevented before starting the 3D printing by preparing the model using the CAD software with appropriate scale factors affecting the dimensional accuracy. Such scale factors include binder saturation, layer thickness, and delay in printing, orientation and moisture level of powder bed.

In order to verify the observed principles and relationships between the dimensional accuracy and the processing factor, a factorial analysis of the variance (ANOVA) was performed and the results are summarized in Table 4(b and c) and Fig. 4(a and b).

According to Table 4(b and c), the first column is the source for each sum of squares of deviation; the second column is the corresponding sums of squares (SS); the third and fourth columns present the degrees of freedom (df) and mean squares (MS),

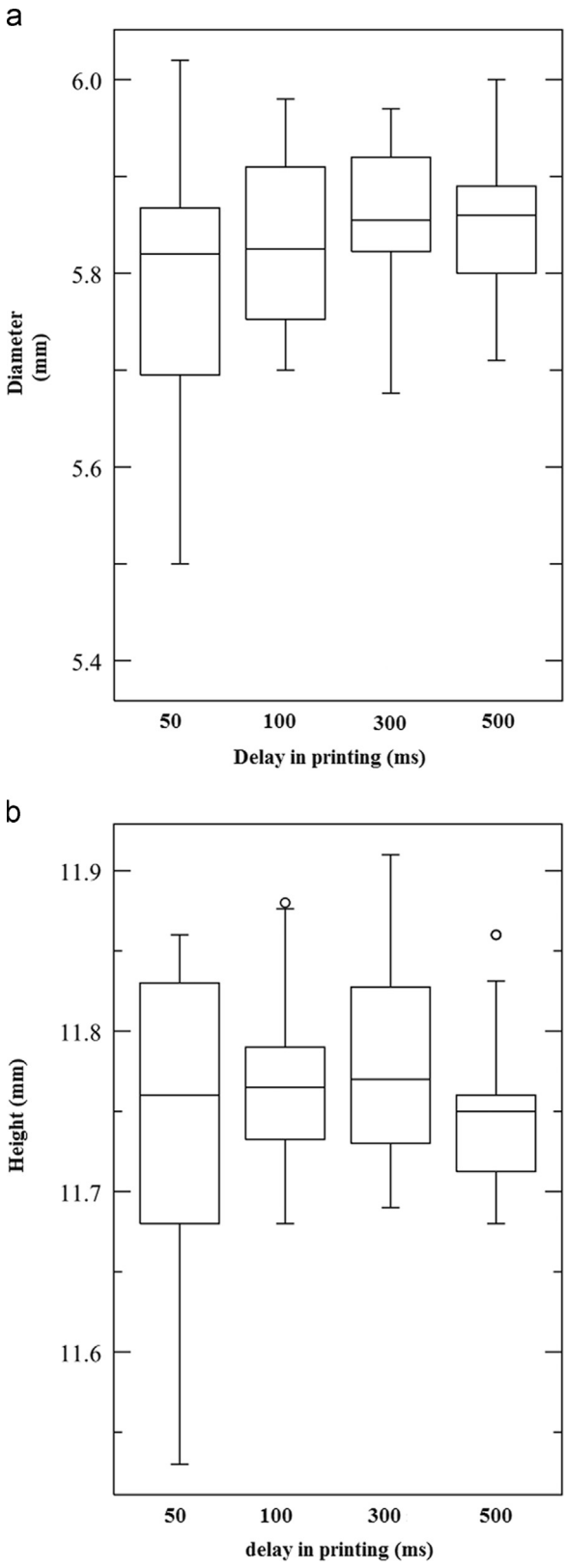

Fig. 4. (a, b): Box-plot of the variability for each group of data, diameter (a) and height (b).

respectively. Also, a calculated value of F used in verifying the equality of treatment methods is presented in the fifth column. As shown, the variances in the processing factor (delay in layer printing) indicate only a minor effect on the height dimension but present a significant effect on the resulting diameter dimension. Furthermore, it was determined that the results of the dimensional testing were highly significant with p values less than 0.05.

As it can be seen in Fig. 4(a and b), the diameter of S_{300} samples are larger compared to other groups in the first and third quartiles with approximate values of 5.83 and 5.92 mm, respectively. Furthermore, S_{50} samples shows a relatively broad range of measured diameters with less accuracy compared to other S_{100}, S_{300} and S_{500} samples. Also, the heights of S_{300} samples are larger in the first; second, third, minimum and maximum measurements. This indicates a close correlation with respect to the height from CAD design.

3.4. Mechanical properties

Mechanical strength is a main concern in porous scaffolds. It is primarily controlled by the pore size, porosity and pore distribution. It still remains a challenge to build strong enough 3D printed scaffolds while a large volume of pores is introduced into the ceramic structures that has limited their use to only low-load bearing applications. Therefore, there is a need for developing an effective way to prepare porous ceramics with appropriate mechanical properties for specific applications [15]. The optimized fabrication parameters and post-processing approaches and compositional modifications can improve mechanical properties of ceramic scaffolds. To investigate the effect of layer printing delay on the mechanical properties of green specimens, compression tests were performed on raw Zp150 prototypes.

The compression strength, tangent Modulus (Young's modulus) and toughness of the 3D printed porous samples were calculated and compared with each other to find the appropriate delay time in printing. The same test setup and parameters were used for all other samples. Five cylinders of each type with 6 mm in diameter and 12 mm in height were used for mechanical properties investigation. Furthermore, calcium sulfate scaffolds demonstrated lower compressive strength, compressive modulus and toughness than those reported for cancellous bones since they were not subjected to any post hardening process [38,41]. The compressive stress–strain curves shown in Fig. 5 are characterized by initial non-linear toe region followed by the main linear region and then the concave shape till the failure point. The average values of five measurements are summarized in Figs. 6–8. The compressive strength, elastic modulus and toughness of the porous scaffolds were quantified from the maximum stress, the initial slope of the linear region of the stress–strain curve and the surface area under the curve, respectively. The fluctuations observed in this region could be attributed to the layer by layer collapse of the microstructure under the compression load.

According to the compressive stress–strain curves in Fig. 5, scaffolds initially underwent the elastic displacement followed by the failure in struts. Based on visual observations, micro-crack generations were occurred in the periphery wall of the scaffolds through the horizontal struts. Moreover, the location of failures is not concentrated in the middle of the scaffolds.

Table 4
(a–c) The average diameter and height of 24 samples for each group with layer thickness of 0.1125 mm with different delay in layer printing (a), ANOVA results of diameter measurement (b), ANOVA results of height measurements (c).

(a)

D1	D2	H	D1	D2	H
50 ms			**100 ms**		
5.8	5.78	11.74	5.83	5.82	11.76
5.79			5.83		
300 ms			**500 ms**		
5.85	5.86	11.78	5.86	5.85	11.75
5.86			5.86		

(b)

Source of variations	(SS)	(DF)	(MS)	*F* value
Between groups	7.2360*E*−02	3	2.4120*E*−02	3.039
Within groups	1.333	168	7.9364*E*−03	
Total	1.406	171		

(c)

Source of Variations				
Between groups	1.9154*E*−02	3	6.3845*E*−03	1.578
Within groups	0.3318	82	4.0469*E*−03	
Total	0.3510	85		

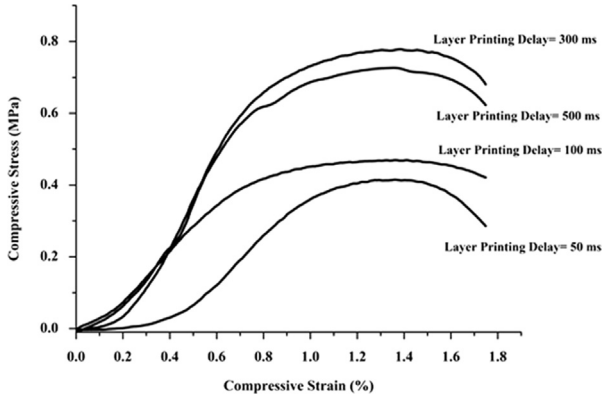

Fig. 5. Compressive stress–strain curve for different layer printing delay of samples printed.

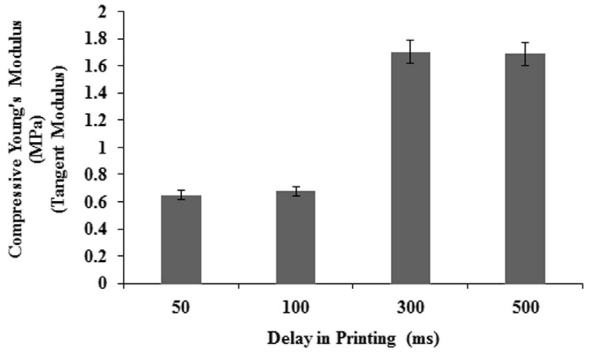

Fig. 7. Comparison of compressive tangent modulus in samples printed with different layer printing delays.

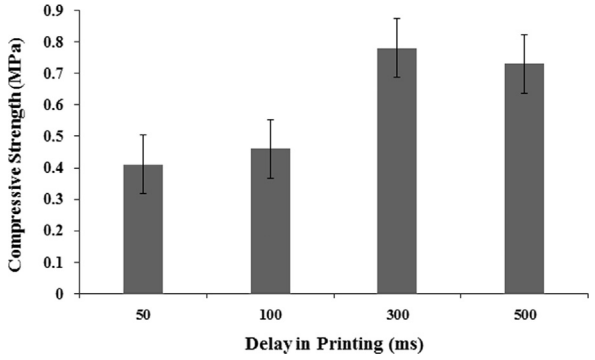

Fig. 6. Comparison of compressive strength in samples printed with different layer printing delays.

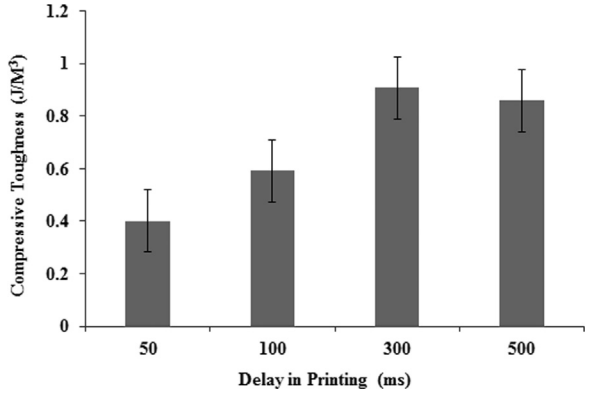

Fig. 8. Comparison of compressive toughness in samples printed with different layer printing delays.

This indicates that the internal structure has a significant influence on the mechanical properties of 3DP samples.

As shown in Fig. 6, difference in printing delays resulted in various compressive strengths. The compressive strength of S_{50} samples were found to be very low for the printed porous samples creating a critical condition for the depowdering and handling steps [30]. S_{300} scaffolds had higher compressive strength. Increasing printing delay from 50 ms to 300 ms increased the compression strength, toughness and tangent modulus of the printed scaffold.

As shown in Figs. 7 and 8, S_{50} scaffolds demonstrated low Tangent modulus and toughness. By increasing the delay to 100, 300 ms and 500 ms, the plastic region was extended, suggesting a higher toughness. As the results indicate, the greatest improvement in compressive strength and toughness were all obtained when scaffolds were printed with a 300 ms delay.

It seems that an increase of delay time results in better binder spreading and uniformity that in turn improves the strength. It is also worthy to note that, also shown in Fig. 6, under the same binder saturation, with an increase of printing delay from 50 ms to 300 ms, the compressive strength would increase. In such cases, as delay time increases, the sprayed binder would penetrate more effectively in vertical and lateral directions over the surface resulting in less empty spaces between the powder particles. This showed that when the saturation level of powders was high, the strength of these specimens increases. This confirms that the incomplete spreading of the binder laterally and vertically would decrease the sample integrity and strength [25]. According to Fig. 6, the weakest average compressive strength was shown by the S_{50} samples. It should be noted that due to the low strength, such samples broke in the depowdering step. In general, S_{300} and S_{500} scaffolds presented higher compressive strength, modulus and toughness in comparison with other scaffolds.

If the printing speed is decreased to less than a limit, previously printed layers are bonded and lowered prior to printing successive layers. So the new layer of powders was not spread uniformly on the surface and some voids and cavities would be created inside the samples. This results in the non-uniformity in scaffold structures. In other cases, it may not be necessary that the binder be fully hardened between layers and a subsequent layer of powder particles may be deposited on a previous layer which is not yet fully hardened. Also, it seems that if the printing speed is increased, the printed layer will have some displacements relative to previously formed layers. So, it may be preferable that the binder harden relatively rapidly upon being deposited so that the next layer of particles placed on a surface of the previous layer is not subject to particle rearrangement due to capillary forces. In printing the samples with considerable delay time, the binder jetting onto the other layers can be completely diffused before the next layer is printed. So, the former layer of powders will be formed more coherently and as a result, the compression strength and dimensional accuracy will be increased. Therefore, finding the optimum delay time in printing is critical for printing porous scaffolds [42,43]. Besides printing delay time, binder drop penetration speed, binder drop penetration depth and binder-powder wetting ratio, should be considered as the affecting factors on printing speed and green strength of the final 3DP components [15].

In general, extremely low or high printing delays can influence the bonding between the powder layers resulting in shearing of the layers during or after the printing process. This in turn lowers the mechanical strength and dimensional accuracy. These results suggest that the delay in printing of samples have a great influence on the mechanical properties of 3DP parts.

Furthermore, the brittleness of the printed samples and the difficulty in predicting their failure was appraised through the common probability distribution calculation like Weibull and exponential distribution. The calculated Weibull modulus of four samples, S_{50}, S_{100}, S_{300} and S_{500}, are 1.262, 1.117, 1.738 and 1.505 respectively. The higher the Weibull modulus is, the more consistent is the material which means that uniform defects are evenly distributed throughout the entire volume. The Weibull distribution is a generalization of an exponential distribution in different ways. It is observed that in many situations exponential distribution provides better fit than a Weibull distribution for brittle samples [44]. The exponential plots for the compressive strength data of the four samples S_{50}, S_{100}, S_{300} and S_{500} are shown in Fig. 9.

It can be found that higher reliability is obtained in the exponential distribution for S_{300} samples, and can be explained by the fact that the 300 ms delay in printing have a higher impact in the fracture mechanism during compression loads, therefore the printed samples are more reliable when subject to 300 ms printing delay [45].

3.5. Tomography and morphological observation

Removal of all loose powders from the 3D printed parts, known as depowdering, was also investigated based on tomography observations using μCT analysis. Based on visual observations, the S_{300} and S_{500} samples have been slightly depowdered compared to other samples. In general, such samples experience less fracture and deterioration compared to S_{50} and S_{100} samples.

Successful bone tissue engineering generally depends on the ability of scaffold to allow diffusion of nutrients and waste removal from the regeneration site. This ability is referred to permeability and it is directly related to the degree of pore interconnectivity. It is also affected by design, particle size and depowdering steps in the fabrication of scaffolds. The removal of the unbound powder from internal features should be seriously considered during the design phase because it will strongly constrain the permeability coefficient, a key parameter in the design of scaffolds [41,46].

Furthermore, the depowdering efficiency was quantified by calculating the solid volume fraction or bone volume density of the printed porous scaffolds from X-Ray μCT data [30]. Bone volume density stands for bone volume over total volume (BV/TV) and indicates the fraction of a given volume of interest (VOI, i.e. the total volume TV) that is occupied by mineralized bone (bone volume). A

cylindrical region of interest (ROI) was set where the scaffolds were located, and the volume of interest (VOI) for all samples was calculated accordingly. The ROI and the total volume (TV) were reduced to the perimeter of the scaffold to quantify the scaffold geometry. This volume was chosen for every single printed scaffold and corresponded to the largest cylinder that could fit into the all morphometric analyses performed within this volume [30,41].

According to the μCT results in Fig. 10(a–c), the lateral view of samples and a middle cross sectional view of a typical scan including layer of powders, pores and struts show that the excess loose powders were effectively removed from the designed pores and provided depowdering was considerable. Moreover, as shown in Table 5, the theoretical values based on CAD models were compared with corresponding measured BV/TV values.

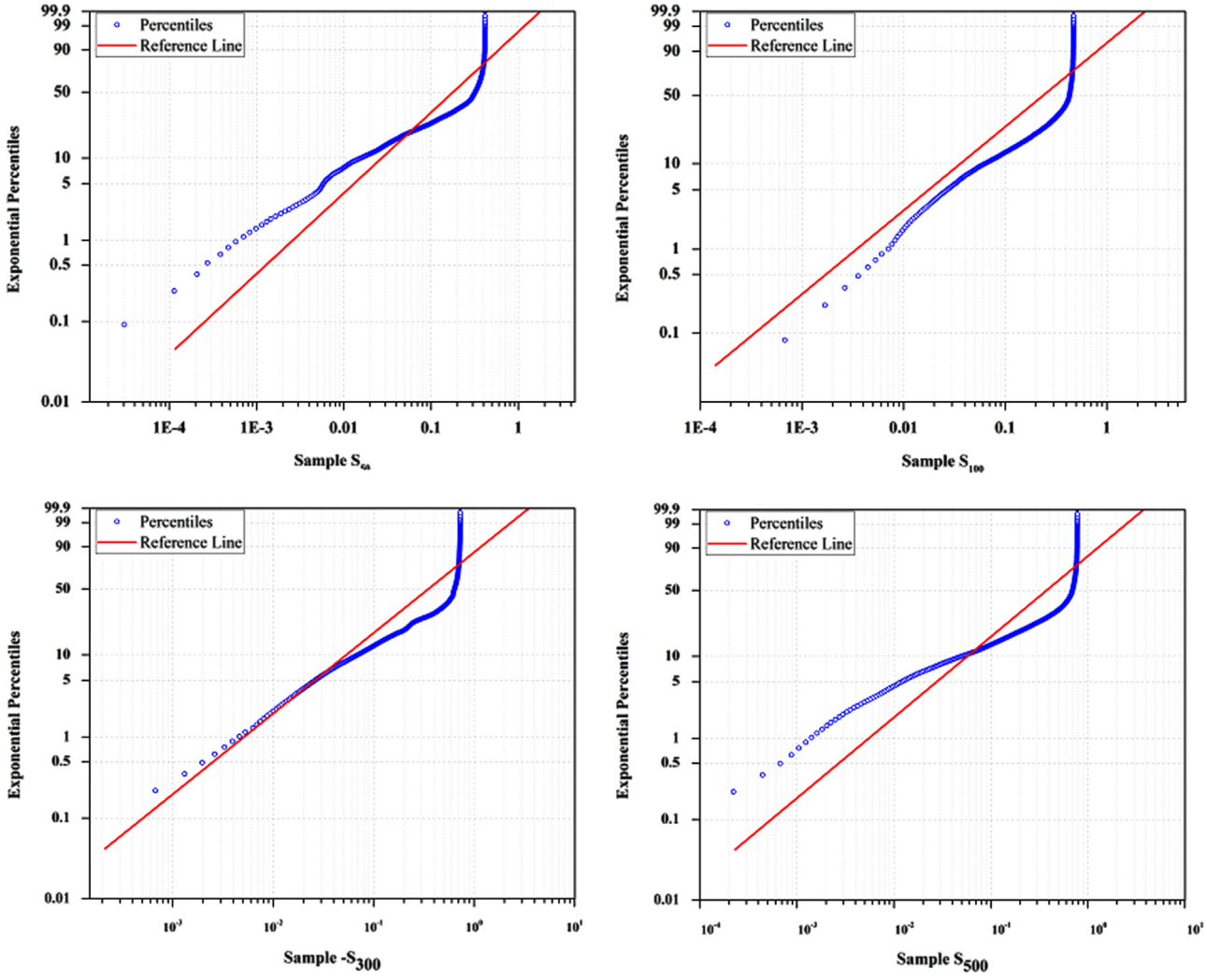

Fig. 9. Exponential probability distribution of samples printed with different layer printing delays.

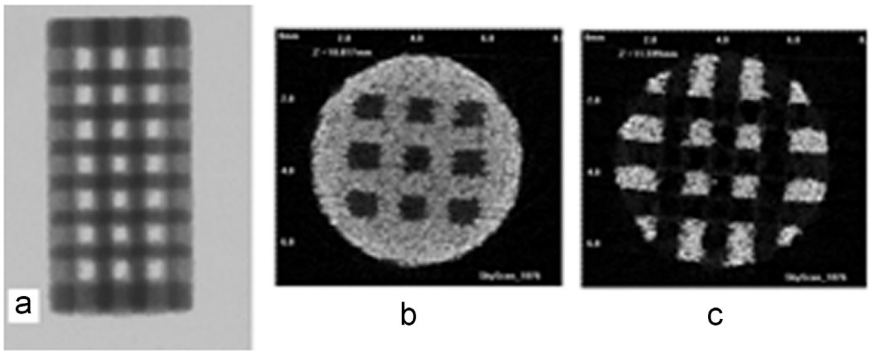

Fig. 10. (a–c): lateral view of samples (a), a middle cross sectional view of a typical scan including layer of powders, pores (b) and struts (c).

Table 5
Comparison of samples' specification between μCT results and CAD design.

Samples' specifications	V_{Porous}/V_{solid} (%)	Macro porosity (%)	Macro pore volume (mm^3)	Connectivity density (mm^{-3})
CAD design	45.05	54.95	186.43	1
μCT data	**Obj.V/TV (%)**	**Total porosity (%)**	**Total pore volume (mm^3)**	**Connectivity density (mm^{-3})**
50	72.44	27.56	95.94	44.78
100	35.23	64.77	231.36	54.95
300	50.41	49.59	169.04	17.03
500	39.47	60.53	213.43	108.51

According to Table 5 and Fig. 11, there was a reduction of about 9.75% in porosity in S_{300} samples compared to other samples with porosity changes in the range of 10.15–49.85%. Furthermore, as shown in Fig. 11, the pore volume was decreased 9.33% (as a minimum) and 48.54% (as a maximum) in S_{300} and S_{50} samples, respectively. The other changes in pore volume of samples were calculated between 14.48% and 24.1% in S_{500} and S_{100} samples, respectively. The comparison of theoretical values (based on CAD models) with measured Obj/TV values confirmed that S_{300} samples had the most significant depowdering. The μCT captures the micro-pore, as well as the macro-porous structure of the design. The micro-pores inside the samples can effect deformation due to the stress concentrations and crack nucleation which result in increasing the probability of fracture under the compression loads. It must be kept in mind that increasing the porosity content or micro-pore size decreased drastically mechanical properties in the samples with the same macropore size and distribution. It seemed likely that the elimination of micro-pores makes an appreciable contribution to the improvement in mechanical properties [47–49]. As shown in Table 6, the specific surface area of sample designed by Solidworks software was 812.21 mm^2. However, the total volume-of-interest (VOI) surface and object surface of 3DP samples were estimated to be in the ranges of 100.61–605.63 mm^2 and 1212.97–3131.54 mm^2 respectively. This difference is attributed to the smooth surface designed by Solidworks software and the rough surface of samples made of powders, (Fig. 12). Also, the difference between object surface and the total VOI can be due to the elimination of the pores in VOI surface.

In porous samples like cancellous bone, the connectivity density has very limited value in assessment of mechanical properties by morphological variables. However, if a relation exists then stiffness and compression strength increases with decreasing connectivity. Connectivity is believed to be an important mechanics-related architectural measure, but very little evidence is available to support this hypothesis [50]. According to Table 5, the S_{300} samples have the lowest connectivity density. It can be in accordance with the highest compression strength and tangent modulus of such samples with respect to the other samples.

The SEM images revealed that the 3D printed samples contained micropores within the microstructure due to the relatively large spacing between the particles ranging between 10 and 30 μm. According to Fig. 12(a), SEM analysis shows a roughened topography on particles. These interlocking crystals

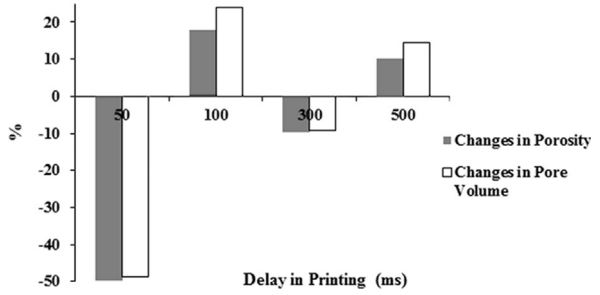

Fig. 11. Porosity reduction and changes in pore volume of samples during printing.

were approximately 40–65 μm. Will et al. reported that for 3DP components, the inter agglomeration pores are generally formed in a size range of 1–100 μm, that agreed well with the observations in our study [46].

According to Fig. 12(b), the macro-pore dimension and strut size are about 700 and 600 μm respectively. They almost match with values in design by Solidworks software with a close approximation. Based on the results of μCT and SEM analyses, the 3D printing can be used to fabricate scaffolds with high accuracy for pore size, pore distribution and pore interconnectivity.

4. Conclusion

The 3D printing method has been recently perceived as a flexible alternative technique to fabricate highly accurate complex shaped scaffolds that were traditionally difficult to build by conventional material processing techniques. This research study demonstrates the low temperature 3D printability of porous scaffolds. The green strength of porous 3D-printed samples comes mainly from the structure affected by printing conditions. Therefore the effects of the layer printing delay on the physical and mechanical properties of the specimens have been studied to better understand and select the most suitable manufacturing parameters. The results suggest that while the layer printing delay has a significant impact on the compressive strength of scaffolds, it has only a minor effect on their structural properties. The scaffolds printed with 300 and 500 ms delays in printing are sufficiently strong for handling and placement into non-loading bone defects. This research study showed that the 300 ms delay in printing was the best printing conditions that offered the highest green strength and dimensional accuracy for ZP150 prototypes.

Table 6
Surface area of both designed and 3DP samples.

Samples	Surface area (mm^2)	
Solidworks software design	812.21	
Delay (ms)	**Total VOI surface (mm^2)**	**Object surface (mm^2)**
50	605.63	2092.25
100	312.16	2805.63
300	300.61	1212.97
500	307.45	3131.54

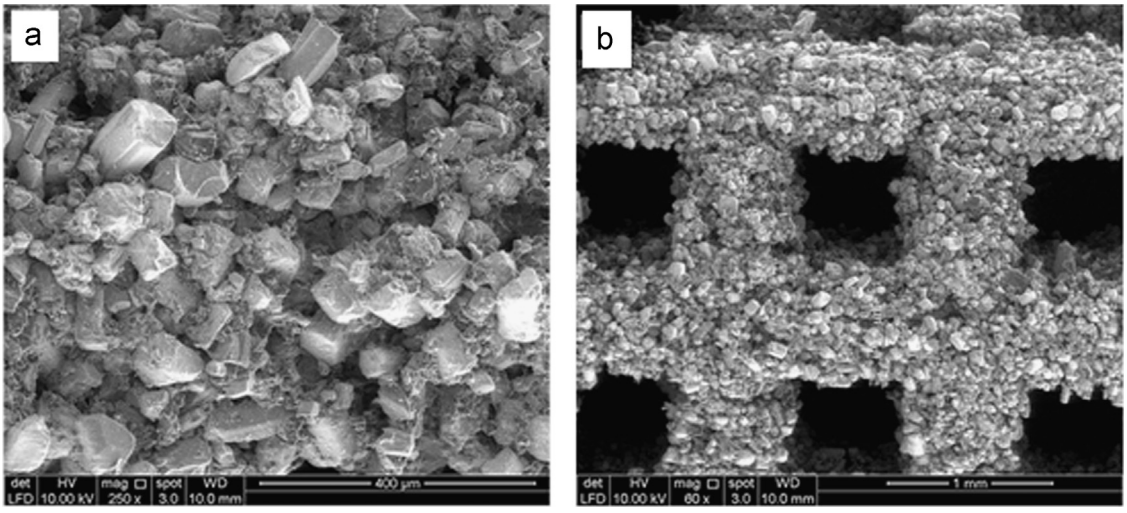

Fig. 12. (a and b): SEM images of powders (a), pores (by design and process) and struts (b) on peripheral wall of samples.

Acknowledgment

This study was supported by High Impact Research UM/MOHE/HIR Project no. D000010-16001. Also, the authors thank all members of Center for Biomedical Technology Integration (CBMTI) for their valuable time and technical assistance.

References

[1] C. Liu, Z. Xia, J. Czernuszka, Design and development of three-dimensional scaffolds for tissue engineering, Chem. Eng. Res. Des. 85 (7) (2007) 1051–1064.
[2] F. Scalera, et al., Influence of the calcination temperature on morphological and mechanical properties of highly porous hydroxyapatite scaffolds, Ceram. Int. 39 (5) (2013) 4839–4846.
[3] S.K. Swain, S. Bhattacharyya, D. Sarkar, Preparation of porous scaffold from hydroxyapatite powders, Mater. Sci. Eng.: C 31 (6) (2011) 1240–1244.
[4] E.-J. Lee, et al., Highly porous hydroxyapatite bioceramics with interconnected pore channels using camphene-based freeze casting, Mater. Lett. 61 (11) (2007) 2270–2273.
[5] N. Monmaturapoj, C. Yatongchai, Influence of preparation method on hydroxyapatite porous scaffolds, Bull. Mater. Sci. 34 (7) (2011) 1733–1737.
[6] M. Castilho, et al., Structural evaluation of scaffolds prototypes produced by three-dimensional printing, Int. J. Adv. Manuf. Technol. 56 (5–8) (2011) 561–569.
[7] G.E. Ryan, A.S. Pandit, D.P. Apatsidis, Porous titanium scaffolds fabricated using a rapid prototyping and powder metallurgy technique, Biomaterials 29 (27) (2008) 3625–3635.
[8] S.M. Peltola, et al., A review of rapid prototyping techniques for tissue engineering purposes, Ann. Med. 40 (4) (2008) 268–280.
[9] J. Wieding, A. Wolf, R. Bader, Numerical optimization of open-porous bone scaffold structures to match the elastic properties of human cortical bone, J. Mech. Behav. Biomed. Mater. 37 (0) (2014) 56–68.
[10] A. Butscher, et al., Printability of calcium phosphate powders for three-dimensional printing of tissue engineering scaffolds, Acta Biomater. 8 (1) (2012) 373–385.
[11] S. Kumar, J.-P. Kruth, Composites by rapid prototyping technology, Mater. Des. 31 (2) (2010) 850–856.
[12] R. Chumnanklang, et al., 3D printing of hydroxyapatite: effect of binder concentration in pre-coated particle on part strength, Mater. Sci. Eng.: C 27 (4) (2007) 914–921.
[13] T. Billiet, et al., A review of trends and limitations in hydrogel-rapid prototyping for tissue engineering, Biomaterials 33 (26) (2012) 6020–6041.
[14] W. Liu, et al., Application and performance of 3D printing in nanobiomaterials, J. Nanomater. 2013 (2013) 1–7.
[15] Z. Zhou, et al., Printability of calcium phosphate: calcium sulfate powders for the application of tissue engineered bone scaffolds using the 3D printing technique, Mater. Sci. Eng. C: Mater. Biol. Appl. 38 (0) (2014) 1–10.
[16] S. Maleksaeedi, et al., Property enhancement of 3D-printed alumina ceramics using vacuum infiltration, J. Mater. Process. Technol. 214 (7) (2014) 1301–1306.

[17] R.A. Watson, A low-cost surgical application of additive fabrication, J. Surg. Educ. 71 (1) (2014) 14–17.
[18] M.T. Stickland, S. McKay, T.J. Scanlon, The development of a three dimensional imaging system and its application in computer aided design workstations, Mechatronics 13 (5) (2003) 521–532.
[19] B. Berman, 3-D printing: the new industrial revolution, Bus. Horiz. 55 (2) (2012) 155–162.
[20] Y. Shanjani, et al., Mechanical characteristics of solid-freeform-fabricated porous calcium polyphosphate structures with oriented stacked layers, Acta Biomater. 7 (4) (2011) 1788–1796.
[21] B. Leukers, et al., Hydroxyapatite scaffolds for bone tissue engineering made by 3D printing, J. Mater. Sci.: Mater. Med. 16 (12) (2005) 1121–1124.
[22] C. Wu, et al., 3D-printing of highly uniform $CaSiO_3$ ceramic scaffolds: preparation, characterization and in vivo osteogenesis, J. Mater. Chem. 22 (24) (2012) 12288–12295.
[23] S. Yang, et al., Rapid prototyping of ceramic lattices for hard tissue scaffolds, Mater. Des. 29 (9) (2008) 1802–1809.
[24] X. Yan, P. Gu, A review of rapid prototyping technologies and systems, Comput. Des. 28 (4) (1996) 307–318.
[25] M. Vaezi, C.K. Chua, Effects of layer thickness and binder saturation level parameters on 3D printing process, Int. J. Adv. Manuf. Technol. 53 (1–4) (2011) 275–284.
[26] M. Castilho, et al., Direct 3D powder printing of biphasic calcium phosphate scaffolds for substitution of complex bone defects, Biofabrication 6 (1) (2014) 015006.
[27] C. Bergmann, et al., 3D printing of bone substitute implants using calcium phosphate and bioactive glasses, J. Eur. Ceram. Soc. 30 (12) (2010) 2563–2567.
[28] A. Butscher, et al., Moisture based three-dimensional printing of calcium phosphate structures for scaffold engineering, Acta Biomater. 9 (2) (2013) 5369–5378.
[29] A. Farzadi, et al., Effect of layer thickness and printing orientation on mechanical properties and dimensional accuracy of 3D printed porous samples for bone tissue engineering, PloS one 9 (9) (2014) e108252.
[30] A. Butscher, et al., New depowdering-friendly designs for three-dimensional printing of calcium phosphate bone substitutes, Acta Biomater. 9 (11) (2013) 9149–9158.
[31] R. Olszewski, P. Szymor, M. Kozakiewicz, Accuracy of three-dimensional, paper-based models generated using a low-cost, three-dimensional printer, J. Cranio-Maxillofac. Surg. (2014).
[32] H.R. Ramay, M. Zhang, Biphasic calcium phosphate nanocomposite porous scaffolds for load-bearing bone tissue engineering, Biomaterials 25 (21) (2004) 5171–5180.
[33] S. Eve, et al., Microstructural and mechanical behaviour of polyamide fibre-reinforced plaster composites, J. Eur. Ceram. Soc. 22 (13) (2002) 2269–2275.
[34] A. Khalyfa, et al., Development of a new calcium phosphate powder-binder system for the 3D printing of patient specific implants, J. Mater. Sci.: Mater. Med. 18 (5) (2007) 909–916.
[35] J. Suwanprateeb, W. Suvannapruk, K. Wasoontararat, Low temperature preparation of calcium phosphate structure via phosphorization of 3D-printed calcium sulfate hemihydrate based material, J. Mater. Sci.: Mater. Med. 21 (2) (2010) 419–429.
[36] T. Galeta, M. Kljajin, M. Karakašić, Geometric accuracy by 2-D printing model, Stroj. vestn. – J. Mech. Eng. 10 (54) (2008) 725–733.
[37] J. Suwanprateeb, et al., Influence of printing parameters on the transformation efficiency of 3D-printed plaster of paris to hydroxyapatite and its properties, Rapid Prototyp. J. 18 (6) (2012) 490–499.
[38] Z. Zhou, et al., Effects of heat treatment on the mechanical and degradation properties of 3D-printed calcium-sulfate-based scaffolds, ISRN Biomater. 2013 (2012) 1–10.
[39] W. Wang, et al., Influence of process parameters on stereolithography part shrinkage, Mater. Des. 17 (4) (1996) 205–213.
[40] Q. Huang, et al., Optimal offline compensation of shape shrinkage for 3d printing processes, IIE Trans. (2015). http://dx.doi.org/10.1080/0740817X.2014.955599.
[41] M. Castilho, et al., Fabrication of computationally designed scaffolds by low temperature 3D printing, Biofabrication 5 (3) (2013) 035012.
[42] E.M. Sachs, et al., Three-dimensional printing techniques, Google Patents, 1994.
[43] M. Cima, et al., Three-dimensional printing techniques, Google Patents, 1995.
[44] R.D. Gupta, D. Kundu, Discriminating between Weibull and generalized exponential distributions, Comput. Stat. Data Anal. 43 (2) (2003) 179–196.
[45] M. Castilho, et al., Application of a 3D printed customized implant for canine cruciate ligament treatment by tibial tuberosity advancement, Biofabrication 6 (2) (2014) 025005.
[46] J. Will, R. Detsch, A.R. Boccaccini, Chapter 7.1 – structural and biological characterization of scaffolds, in: A. Bandyopadhyay, S. Bose (Eds.), Characterization of Biomaterials, Academic Press, Oxford, 2013, pp. 299–310.
[47] H. Li, et al., Effects of pore morphology and bone ingrowth on mechanical properties of microporous titanium as an orthopaedic implant material, Mater. Trans. 45 (4) (2004) 1124–1131.
[48] H. Toda, et al., Effects of hydrogen micro pores on mechanical properties in A2024 aluminum alloys, Mater. Trans. 54 (12) (2013) 2195–2201.
[49] A. Bignon, et al., Effect of micro-and macroporosity of bone substitutes on their mechanical properties and cellular response, J. Mater. Sci.: Mater. Med. 14 (12) (2003) 1089–1097.
[50] J. Kabel, et al., Connectivity and the elastic properties of cancellous bone, Bone 24 (2) (1999) 115–120.